Astronomical and Astrophysical Transactions (*AApTr*), 2025, Vol. 35, Issue 4, pp. 493–500,
ISSN 1055-6796, Photocopying permitted by license only, ©Cambridge Scientific Publishers

Optical microvariability as a tool for investigating the internal structure of the jet flow

M.A. Gorbachev*, M.S. Butuzova

Crimean Astrophysical Observatory, Nauchny, 298409, Russia

Received 15 June, 2025; accepted 28 August, 2025

The compact region of blazar's optical radiation is inaccessible for observations using aperture synthesis antennas. This radiation shows variability on different time scales. One of the reasons for the observed blazar's variability is the change in the coefficient of relativistic boosting (Doppler factor) caused by changes in the velocity and/or motion direction relative to the observer. We believe that the appearance and evolution of subcomponents with a different Doppler factor from that of the main part of the radiating region give rise to a variability on short time scales. Based on these assumptions, we constructed a geometric scheme of the optical emitting region and implemented an algorithm to simulate the light curves under this scenario.

This allowed us to reproduce the light curves that are qualitatively similar to the observed ones. The power spectrum densities (PSD) based on these data agree well with values from observed data of the blazar S4 0954+65 ($-2.3 < \boldsymbol{\alpha} < -1.7$, $\log(\nu_{\rm break}) \sim -3.6$ [Hz]). Within the framework of this model, it is shown that the break and flat spectrum at high frequencies in PSD are due to the strong influence of photometric noise.

Keywords: Galaxies: active, Galaxies: jets, quasars: general, Instrumentation: photometers, Methods: data analysis

1 Introduction

Blazars are active galactic nuclei (AGNs) whose ultrarelativistic jet is directed toward the observer at a small angle (<10°). Due to relativistic effects, the radiation generated in the jet is boosted in the observer's reference frame and outshines the radiation from the rest of the AGN. The record-breaking angular resolution achieved by very long baseline interferometry (VLBI) in the radio range makes it possible to observe jets on spatial scales of parsecs (e.g., Lister et al., 2021). In regions close to the true jet base, synchrotron self-absorption is active (Pushkarev et al., 2012), the effect of which decreases with increasing frequency. Therefore, the optical emission comes from a compact region located upstream of the observed jets by the VLBI. There are

*Email: mgorbachev17@gmail.com

two reasons for the observed blazar variability. The first one is the physical changes in the jet flow, for example, the acceleration of electrons at shock wave fronts. The second one is a change in the relativistic boosting coefficient δ (Doppler factor) due to changes in the jet's velocity and/or motion direction relative to the observer. The latter may significantly affect the variability. In fact, Lister et al. (2021) detected the jet components moving along a curved trajectory on parsec scales, which will certainly affect the local variation of the jet components' Doppler factors. Moreover, Mertens et al. (2016) revealed a motion along helical trajectories in the flow for the jet of the nearest AGN M 87. Therefore, before evaluating the physical parameters of blazar jets, it is necessary to understand what contribution the change in the Doppler factor makes to the overall variability of the radiation flux.

A change in δ of the entire radiative region leads to variability on long time scales (see, e.g., Gorbachev et al., 2024). On a short time scale, the variability can be caused by the appearance and evolution of sub-components of the flow with Doppler factors that differ from the δ of the emitting region main part (Butuzova et al., 2025). This sub-component is part of the radiating region that moves at a certain angle to the general trajectory. In this article, we model this scenario for the formation of short-term variability and analyze its applicability to the interpretation of real data.

2 Simulation

To simulate, we introduce a geometry scheme of the considered variability scenario. The optical emitting region is represented as a truncated cone with a length of R, a radius of the upper base of r_0, and an angle of taper of χ (Fig. 1). At some point in time, due to various inhomogeneities or the development of instabilities, sub-components are formed in the jet's matter flow, moving along curved trajectories (Fig. 1, bold blue line) at a certain angle to the general motion direction (angle ρ) and, as a result, characterized by a changing δ. Let us consider whether the superposition of the emission of these sub-components will lead to the short-term variability observed in the optical range.

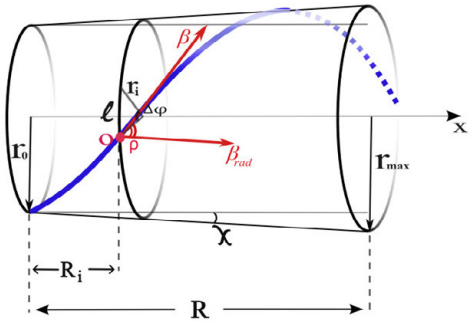


Figure 1 Geometric scheme of the motion of the sub-component (curved line) in the jet flow. The dotted line is the trajectory of movement from the back of the jet relative to the observer. The parameters are described in Table 1.

In the first stage, the initial parameters of the model are set, including the total number of sub-components (N, a random number; optimal values are typically between 10^2 and 10^3). We suppose that the main component is characterized by a constant spectral flux density ($F_{\rm main}$; in the following text, for brevity, the term "flux" will be used instead of "spectral flux density") in the observer's reference frame, a spectral index ($a_{\rm main}$, $F \sim \nu^{-a}$), and a relativistic Doppler factor ($\delta_{\rm main}$). In such a case, from the equation for flux

$$F = Q \cdot \nu^{-a} \cdot \delta^{3+a} \tag{1}$$

we can estimate the value of the normalization parameter $Q(n, B, V)$, which depends on the particle concentration n, magnetic field B, and volume V. The value of $\delta_{\rm main}$ is determined from the general relation with the corresponding substitution:

$$\delta = \frac{\sqrt{1-\beta^2}}{1-\beta \cdot \cos(\theta)}, \tag{2}$$

where $\beta = v/c$, c is the speed of light, v is the component velocity, and $\theta = \theta_0$ is the angle between the line of sight and the cone axis. Each sub-component is characterized by the time of occurrence (t_0), the distance from the cone axis (r_0), the value D, which determines the normalization coefficient for the flux of a sub-component $Q_{\rm sub} = D \cdot Q$, as well as other geometric parameters (χ, φ_0, ρ). A whole description of these parameters is provided in Table 1.

At the second stage, the change in δ of the sub-component over time is calculated, which makes it possible to obtain a light curve in the observer's reference frame. To do this, using equation (1), the θ value is calculated for each time point (Butuzova, 2018):

$$\theta(\mathrm{t}) = \arcsin\sqrt{f_{\rm a}^2 + f_{\rm b}^2}, \tag{3}$$

$$f_{\rm a} = \cos\rho \sin\chi \sin\varphi(\mathrm{t}) + \sin\rho\cos\varphi(\mathrm{t}),$$

$$f_{\rm b} = \cos\rho(\cos\chi\sin\theta_0 + \sin\chi\cos\theta_0\cos\varphi(\mathrm{t})) - \sin\rho\cos\theta_0\sin\varphi(\mathrm{t})$$

considering that $\varphi(t_i) = \varphi(t_{i-1}) + \Delta\varphi_i$, where $\Delta\varphi_i = \beta\sin\rho/r_i$. Substituting the obtained values of $\theta(t)$ into equation (2), the δ of the sub-component is determined. We assume the relative velocity of the main flow and the sub-component is equal to $\beta = 0.99$. By applying the transformation $\Delta\mathrm{t} = \Delta\mathrm{t}'\delta$, where $\Delta\mathrm{t}$ is the time interval between neighboring observation points, and the prime means the source's reference frame, we obtain the light curve of the sub-component in the observer's reference frame. So, this algorithm constructed a set of light curves for all sub-components.

At the final stage, we obtain the total light curve. For this, all the light curves from the set are added as follows:

$$F(\mathrm{t}_i) = F_{\rm main}(\mathrm{t}_i) + \sum_{j=1}^{N} F_{\mathrm{sub}_j}(\mathrm{t}_i), \tag{4}$$

Table 1 Simulation parameters.

Name	Value	Unit of measurement	Annotation
c	$3 \cdot 10^{10}$	cm/s	Speed of light
β	0.99	–	Relative velocity
θ_0	5	deg	Angle of the jet axis with the line of sight.
F_{main}	1	mJy	Flux of the main component.
a_{main}	1.5	–	Spectral index of the main component.
ν	$4.29 \cdot 10^{14}$	Hz	Frequency of the filter for which the simulation is performed corresponds to the frequency of the R band.
δ_{main}	$\delta_{\text{main}}(\beta, \theta_0)$	–	Doppler factor of the main component.
R	$5 \cdot 10^{-2}$	pc	Length of the radiating region.
r_0	$5 \cdot 10^{-4}$	pc	Initial radius of the radiating region
D	$[0.001, 0.3]$	–	Normalization coefficient of the sub-component expressed in fractions of the parameter Q of the main component.
t_0	$[0, \infty]$	hour	The time when the sub-component appears in the source's reference frame. Randomly generated in the range from 0 to t.
ρ	$[1, 10]$	deg	Angle of deviation of the sub-component motion from the radial direction. It is set randomly within the range.
φ_0	$[0, 360)$	deg	The initial azimuth angle of the sub-component. It is set randomly.
χ	$[1, 4]$	deg	The angle between the cone generatrix along which the sub-component moves and the overall motion direction. It is set randomly.
d_{R}	$[0, 0.9]$	–	A fraction of the emitting region radius
R_0	$d_{\text{R}} \cdot R$	pc	Distance from the emitting region's beginning to the sub-component's point of appearance along the emitting region.
d_{r}	$[0.1, 1]$	–	A fraction of the emitting region radius. It depends on the D parameter: $d_{\text{r}} \propto 1/D$
r	$d_{\text{r}} \cdot r_0$	pc	The distance from the emitting region center, where the sub-component is formed.
N	≥ 1	–	Total number of sub-components in the model.

where t_{i} is the time value in the observer's reference frame, and j is the index of the sub-component. If there is no data for the sub-component at time t_{i}, but there is data for neighboring points $(t_{\text{i-1}}, t_{\text{i+1}})$, then a linear approximation is performed for time t_{i}. The time resolution can vary from 1 minute to several hours or days, but it is advisable to set it in the range from 10 minutes to 1 hour. In real observational data, increasing the time resolution leads to a higher contribution of Poisson (photometric) noise to the light curves. This is visible in the data obtained by the TESS orbital observatory (Ricker et al., 2015), with a resolution of better than 10 min. Therefore, for high-resolution models in equation (4), we introduce the noise component $W{\cdot}Noise$, where $Noise$ is the photometric noise level, and W is a normalization factor taking values from 0 to 1, which allows us to adjust the effect of noise on the light curve.

This concludes the description of the algorithm that makes it possible to obtain the light curve of the optical emitting region within the framework of our assumptions. In the next section, we present and discuss the simulation results.

3 Results

Having selected the optimal simulation parameters (see Table 1), we calculated 100 models with a time resolution of 10 and 60 min, as well as various contributions of Poisson noise to data with a 10-min resolution. Figure 2 shows examples of model light curves. The change in the azimuthal angle of the sub-components during their existence ranges from several degrees to several tens of degrees ($< 25°$). Thus, this means that they do not have enough time to make a complete revolution around the radiating region. To verify the correspondence of the obtained models with the observed blazar's light curves, we constructed a power spectral density (PSD) for each model. The resulting PSDs were binned in increments of $\log(\nu) = 0.1$ Hz and used linear regression with χ^2 error statistic minimization to fit them with a broken power-law up to the Nyquist frequency $\nu_{\rm N}$. If there was no break in the PSD, then a linear approximation of the spectrum to $\nu_{\rm N}$ was performed. In each group of models, the median value of the slope of the power spectrum and the break frequency, if present, as well as the corresponding error, were calculated. The range of the obtained power spectral slope values for the model light curves ($-2.3 < \boldsymbol{\alpha} < -1.7$) is consistent with the results for the source S4 0954+65 based on TESS data, within the uncertainties (Raiteri et al., 2021).

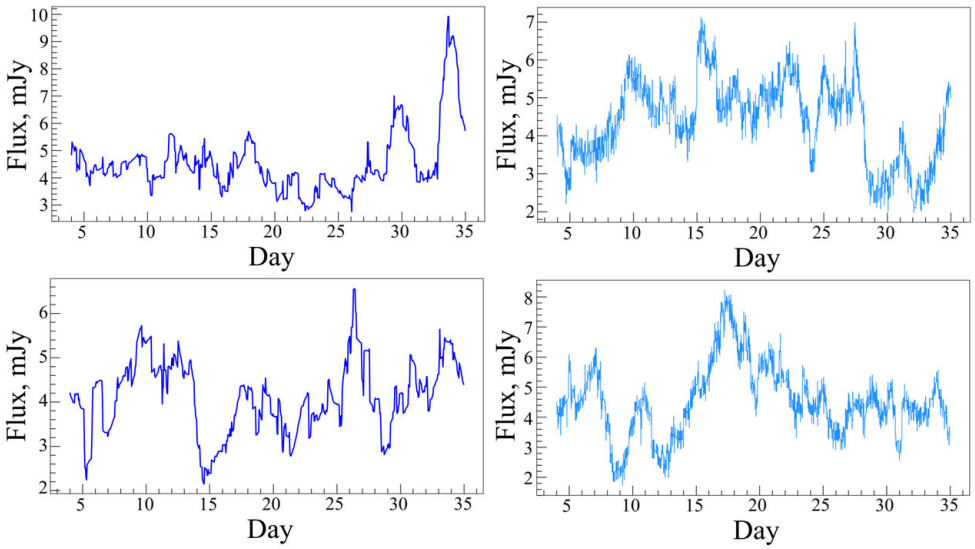


Figure 2 Examples of model light curves with a time resolution of 10 (left panel) and 60 minutes (right panel). The graphs on the upper and lower panels differ in parameters, primarily t_0, φ_0, R_0, and others.

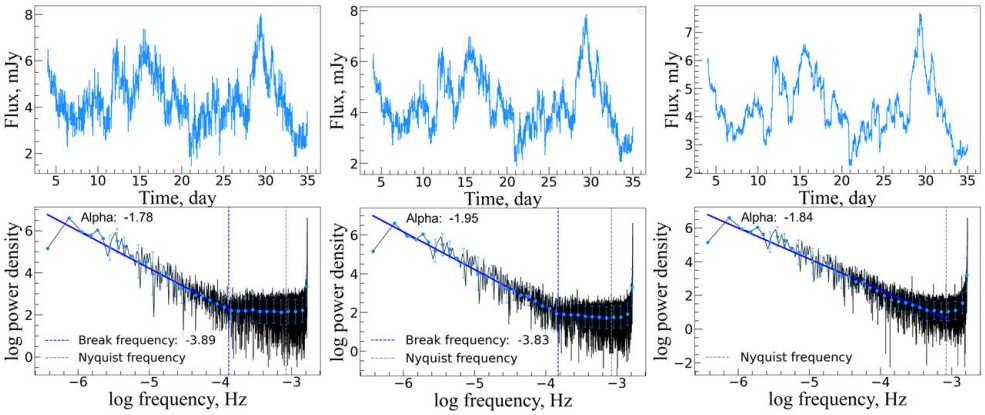


Figure 3 Model light curves (upper panel) and their corresponding PSD (lower panel) for various values of W (from left to right: 0.5, 0.3, 0.1). The vertical dashed gray lines mark the Nyquist frequency. The solid blue line represents a broken power-law fit (left and middle panels) or a simple power-law fit (right panel) corresponding to the PSD and binned in steps of $\log f = 0.1$ up to the Nyquist frequency. The vertical dashed blue lines indicate the best-fitting break frequency.

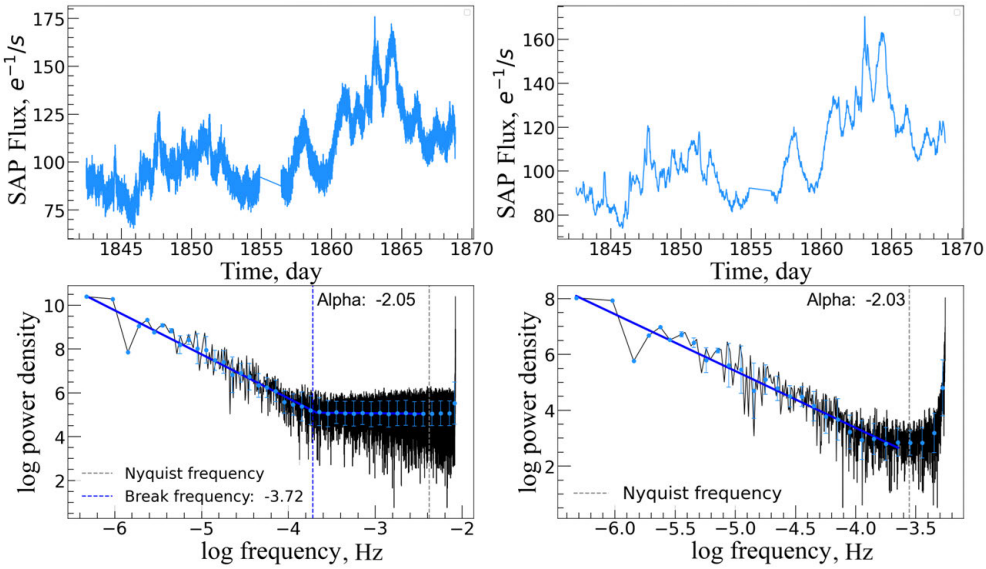


Figure 4 The top panel shows the light curves of the blazar S4 0954+65 from TESS sector 20 at 120-s (left) and 1800-s (right) time resolution. Bottom panel: PSDs corresponding to the light curves in the top panel.

To study the effect of Poisson noise, we calculated models for three values of the noise component parameter W. Figure 3 shows three light curves and their corresponding power spectra for values of $W = 0.5, 0.3$, and 0.1, respectively. The graphs

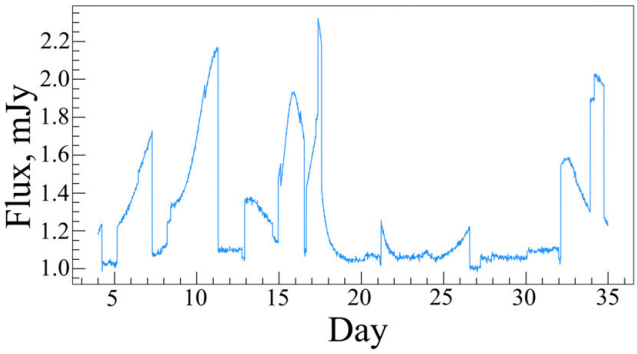


Figure 5 Model light curve for a small number of sub-components ($N = 50$).

clearly show that a high noise level significantly affects the high-frequency region of the spectrum, thereby distorting the true power spectrum and causing a break to appear, with its frequency shifting to lower values with growth noise contribution. In their study, Raiteri et al. (2021) used TESS data with a 2-minute time resolution. As a result of PSD analysis, the break frequency was determined to be $\log(\nu_{\rm break}) = -3.77 \pm 0.24, -3.70 \pm 0.27$, and -3.61 ± 0.30 [Hz] for sectors 14, 20, and 21, respectively. We also modeled data with the same time resolution, which is qualitatively similar to the TESS light curves. The break ($\log(\nu_{\rm break}) \sim -3.6$ [Hz]) observed in our data is caused solely by noise and is close to the lower bound of the break frequency obtained by Raiteri et al. (2021). Thus, we assume that the break in the data used by Raiteri et al. (2021) may be caused by Poisson noise rather than physical processes. To illustrate our hypothesis, we analysed the light curve of the blazar S4 0954+65 obtained by the TESS with time resolutions of 120 and 1800 seconds from sector 20 (Fig. 4, upper panel). We also computed the PSD for these data using the method described above (Fig. 4, lower panel). As can be seen from the figure, the PSD for the light curve with a time resolution of 1800 seconds shows no break, while the data with higher time resolution clearly show a break.

Moreover, it should be noted that using too few sub-components results in voids and irregular, sparse peaks (Fig. 5). In our simulation, we used $R = 5{\cdot}10^{-2}$ parsecs, which corresponds to the data from other studies (e.g. Dingler et al., 2024). With these parameters, the optimal number of sub-components ranges from 10^2 to 10^3.

4 Conclusions

The model developed by us demonstrates high efficiency due to flexible parameter settings, which allows reproducing light curves that are qualitatively similar to the observed ones. The slope of the power spectrum density lies in the range from –2.3 to –1.7, which corresponds to the observed data. The analysis of the model parameters shows that the observed variability on short time scales is not due to the "rotation" of a sub-component around the emitting region, but rather arises from a combination of continuously varying numbers of sub-components with different parameters. In

addition, the use of high-noise observational data, such as TESS light curves for blazars, leads to a break in the power spectrum that is not related to the object's physics.

The continuation of this work consists of developing a method for comparing the power spectra of the model and observed light curves, taking into account their distortion due to the limitations of the observational series. It is also of particular interest to perform the inverse task: to obtain various model parameters based on observational data. Thus, we'll get a powerful tool for studying the internal structure of the blazar jet flow.

Acknowledgements

This work was supported by the Russian Science Foundation, No. 24-22-00343.

References

Butuzova M.S. (2018) ARep, 62, 116
Butuzova M.S., Guseva V.A., Gorbachev M.A., et al. (2025) JHEP, 45, 19
Dingler R., Smith K.L. (2024) ApJ, 973, 10
Gorbachev M.A., Butuzova M.S., Nazarov S.V., et al. (2024) APh, 160, id.102965
Lister M.L., Homan D.C., Kellermann K.I., et al. (2021) ApJ, 923, id.30
Mertens F., Lobanov A.P., Walker R.C., Hardee P.E. (2016) A&A, 595, A54
Pushkarev A.B., Hovatta T., Kovalev Y.Y., et al (2012) A&A, 545, A113
Raiteri C.M., Villata M., Larionov V.M.., et al. (2021) MNRAS, 504, 5629
Ricker G.R., Winn J.N., Vanderspek R., et al. (2015) Journal of Astronomical Telescopes, Instruments, and Systems, 1, id.014003